Research Article | Vol. 27, No. 2 | 21 Jan 2019 | OPTICS EXPRESS 1750
Optics EXPRESS

Characterization of radiance from the ocean surface by hyperspectral imaging

CARLOS CARRIZO,[1] ALEXANDER GILERSON,[1,*] ROBERT FOSTER,[2] ANDRII GOLOVIN,[1] AND AHMED EL-HABASHI[1,2]

[1]*The City College of New York, CUNY, New York, NY 10031, USA*
[2]*Remote Sensing Division, Naval Research Laboratory, Washington, DC 20375, USA*
**gilerson@ccny.cuny.edu*

Abstract: A novel snapshot hyperspectral imager is introduced for ocean color (OC) applications and its capabilities are demonstrated. The instrument provides hyperspectral radiance images with a wide field-of-view (FOV) and short exposure time, which is valuable for the direct characterization of the wind-roughened surface in various illumination conditions and wind speeds. Uncertainties in the total (L_t), sky (L_s) and derived water-leaving (L_w) radiances at viewing angles of 20–60° are determined as a function of wind speed together with associated correlation coefficients and variances of the sea surface reflectance coefficient ρ. Estimated L_w uncertainties can partially explain the inaccuracy of satellite retrievals in the blue bands in the coastal waters. It is shown that in above-water measurements in no-glint conditions with viewing and azimuth angles of 40° and 90°, respectively, for both $L_t(\lambda)$ and $L_s(\lambda)$ the impact of FOV is minimal at least up to measured W = 5.7 m/s for full-angle FOV of 4° and larger. Implications of uncertainties for the derivation of water leaving radiance in above-water ship-borne and AERONET-OC measurements are discussed.

1. Introduction

Multi-spectral remote sensing reflectance data from Ocean Color (OC) satellites are suitable for the retrieval of important water parameters such as concentration of chlorophyll-a, absorption and backscattering coefficients, but they often do not have appropriate spatial and spectral resolution in some applications, such as characterization of the bottom, detection of underwater objects and depth retrieval. Hyperspectral measurements with proper resolution can significantly improve the accuracy of retrievals in complex coastal and inland waters, and are particularly useful in shallow waters where bathymetric and bottom make-up information maps can be retrieved [1].

Development of hyperspectral imagers and applications of hyperspectral imagery to coastal and optically shallow waters has attracted increasing attention. Some example airborne sensors include [2]: AVIRIS, Ocean PHILLS and CASI instruments, and the satellite-borne Hyperion imager. Applications range from validation [3] to mapping and classification of corals [4], extraction of bathymetry and bottom types [5] as well as algorithm development [6,7]. Recent systems include the HICO instrument on the International Space Station [8] and a new generation NASA airborne imager PRISM [9] with multiple applications, which demonstrate the efficacy of hyperspectral imaging [10]. In NASA's Plankton, Aerosol, Cloud, and ocean Ecosystem (PACE) mission [11] it is expected that the main sensor will be a hyperspectral imager, so different aspects of hyperspectral sensing and processing including atmospheric correction [12,13], surface characterization, skylight correction and advanced retrieval algorithms are especially important and require novel approaches.

#345443 https://doi.org/10.1364/OE.27.001750
Journal © 2019 Received 10 Sep 2018; revised 8 Jan 2019; accepted 9 Jan 2019; published 18 Jan 2019

Optics EXPRESS

Until recently, advances in hyperspectral imaging were generally constrained to improvements in signal-to-noise ratio, or increases of cross-track or spectral resolution through substitution of newer generations of focal plane arrays. However the basic design still required physically moving or scanning the instrument to achieve along-track information, the so-called "push-broom" mode of operation. The recent development of "snapshot" mode hyperspectral imagers eliminates this difficulty, and while such instruments have their own disadvantages, measurements can be made from non-moving platforms, ships, etc., providing an abundance of new data and capabilities [14].

In OC applications, the accuracy of retrievals of water parameters depends on the quality of the estimated remote sensing reflectance (R_{rs}). One of the significant uncertainties in this estimation is associated with the characterization of the ocean surface, especially in windy conditions, and removal of the sky component reflected from this surface. For satellite applications, such reflectance is included in the atmospheric correction algorithm, specifically in the calculation of the Rayleigh and aerosol components [15–17]. For ship-borne measurements, the reflectance coefficient of skylight from the sea surface (ρ) is pre-calculated for specific geometries, which are recommended for such observations [18,19]. In all these cases, the impact of the wind-roughened surface on the radiance is estimated based on statistics of Cox and Munk [20], who measured wave slopes as a function of the wind speed. This approach is included in multiple scalar [21] and vector [16,22–26] radiative transfer models and allows simulation of the mean radiance spectra for differing wind speeds and various atmospheric and water conditions. Such models, however, do not estimate the variability of the radiance spectra and corresponding uncertainties in measurements of the water leaving radiance (or R_{rs}) in windy conditions. Several factors drive these uncertainties. Typically, for *in situ* Ocean Color measurements, Cox-Munk statistics (derived from an approximate wind speed measurement) are the only available indicator of the instantaneous sea state. The reflectance coefficient, ρ, depends strongly on knowledge of the sea state, but also significantly on wavelength, aerosol characteristics and polarization effects, which are not routinely measured [24,27–31]. Related uncertainties can affect the quality of the near surface measurements and atmospheric correction [32]. That includes data from AERONET-OC stations [33], which are based on above water measurements from ocean platforms and are widely used for the validation of satellite sensors.

The goal of this paper is to demonstrate the capabilities of a new snapshot hyperspectral imager for applications of interest to the ocean color community, including characterization of the ocean surface, estimation of the uncertainties associated with above water radiometric measurements and derived water leaving radiances.

This paper is broken down as follows: Section 2 introduces the imager, Section 3 describes our uncertainty model for water-leaving radiance, Section 4 describes the *in situ* data collected with the imager, Section 5 combines uncertainty model with the spatial and spectral information of the imager to analyze the sources of uncertainty in the derivation of R_{rs}, Section 6 discusses the implications of the results to above-water, AERONET-OC and satellite retrievals, and Section 7 concludes the work.

2. Instrumentation and calibration

As was mentioned before, hyperspectral imagers which were thus far used in ocean studies were primarily based on a push-broom method of data acquisition, with hyperspectral and cross track data recorded in one CCD scan and with the along track dimension added through the movement of the system. Some instruments attempt to circumvent this requirement through addition of a rotatable mirror, however this is only a partial solution; the resultant system requires additional time to complete a scan, and becomes polarization sensitive.

The Cubert company (Germany) recently developed a robust imaging spectrometer UHD285 (Fig. 1) with no moving parts which permits acquisition of the entire spectral cube

Optics EXPRESS

in the visible/NIR part of the spectrum. Internally, after light from the scene passes through the objective lens, it is divided by a 50:50 cubic non-polarizing beam splitter. One-half is directed to a photo-detector matrix for acquisition of a panchromatic image in the 450-1000 nm wavelength range with a spatial resolution of 1000x1000 pixels. The other half of the beam is modified by a microlens array, collimated, spectrally split using a prism, and finally focused on a second detector matrix. After processing with Cubert's proprietary algorithm, 138 spectral channels with 4 nm spacing are available in a 50x50 pixel image. It was found that the instrument has some polarization sensitivity; however, these effects were not taken into account in the current study.

The entire system can collect images with a frame rate of up to 20 cubes/s and 14 bit digitization. The weight of the instrument is about 3kg and it has dimensions of 280 mm in length and 100 mm in diameter, which makes it suitable for various field measurements.

Since a prism is used as the dispersive element in the imager, the spectral bandwidth strongly depends on the wavelength [34], Fig. 2(a). To illustrate the effects on the measurements, Fig. 2(b) shows a spectrum of a Spectralon plate under clear-sky conditions taken by a GER-1500 spectroradiometer with ≈ 1.5 nm resolution (SpectraVista, NY), compared with the same spectra measured by center pixel of the UHD285 imager. Near Fraunhofer lines or other pronounced absorption peaks, there can be deviations (as with most spectrometers), but the effect becomes much more pronounced as the wavelength increases.

The non-scanning feature eliminates the necessity of the continual movement required by push-broom imagers. This new approach opens the possibility for continuous observations from elevated on-shore locations, and from ocean platforms, as well as from appropriately positioned helicopters. The method can therefore be used for monitoring fast changing features and processes in the ocean and on the surface for any desired period of time, at video frame rates. A UHD285 imager was recently acquired by the Optical Remote Sensing Laboratory at CCNY, where it underwent additional laboratory calibration and was used in field measurements of ocean waters from several platforms. A typical integration time for ocean observations with the imager is 20-50 ms, which means that the images represent an average state of the ocean surface, and are unable to capture fine-scale wave structure, which would require integration times below 1ms [35].

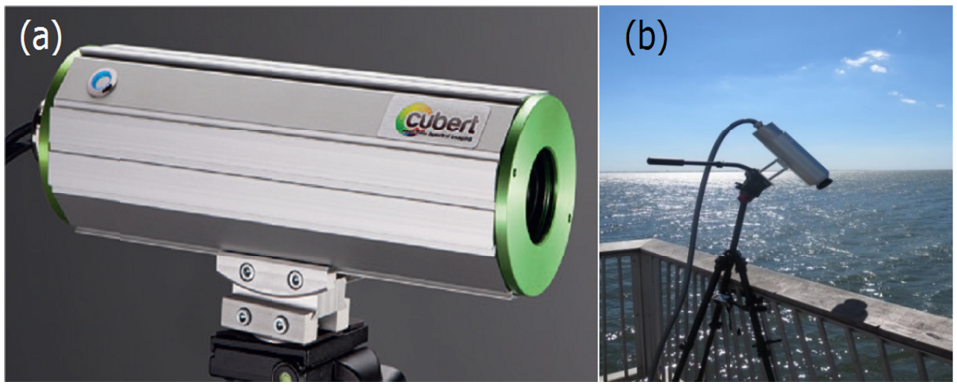

Fig. 1. Snapshot hyperspectral imager Cubert UHD285: (a) general view, (b) on the tripod at the ocean platform.

In our measurements, the system was used with an additional lens in front of the imager, which increased the FOV to 40°. The sophistication of the imager calibration can be seen from Fig. 3, where only two wavelengths are shown. Similar matrices are generated for all 138 wavelengths of the imager. This calibration was carried out through the comparison of radiances reflected from a white Lambertian plate standard (ZenithLite™, SphereOptics GmbH) with the radiances measured by the GER spectroradiometer, which recently underwent spectral and radiometric calibration at the manufacturer.

Optics EXPRESS

For initial field deployments, dark measurements were conducted by manually placing a cap over the aperture. For later deployments, a filter wheel was installed in front of the imager to automate a switch between dark and object measurements, which resulted in small shadowing of light in the corners of the instrument.

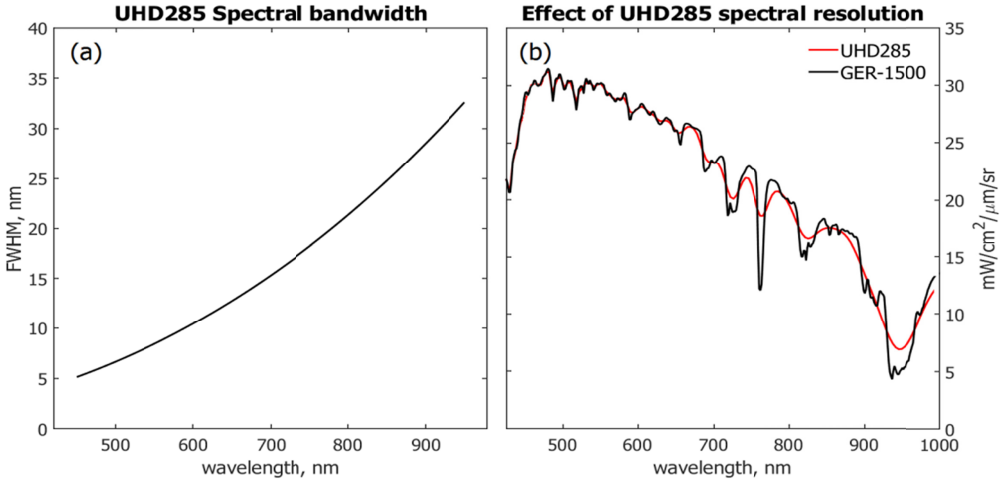

Fig. 2. Integration of the spectra by the imager: (a) spectral bandwidths, (b) comparison with GER spectrum.

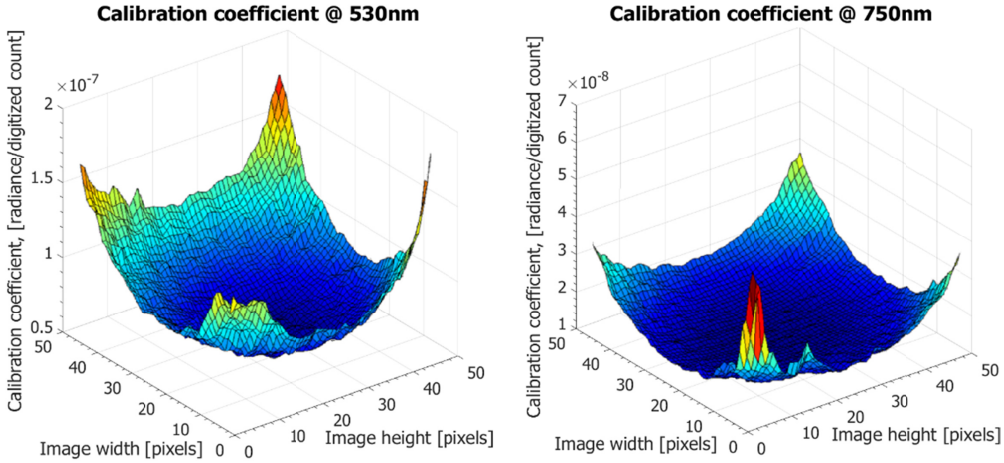

Fig. 3. Calibration matrices for the imager at 530 and 750 nm.

3. Theory and modeling

The related theory was discussed in details elsewhere [31] but is briefly repeated here. The main parameter of interest in the field of OC is the remote sensing reflectance R_{rs} just above the surface of the ocean [36]:

$$R_{rs}(\theta_v, \varphi_v, \lambda) = L_w(\theta_v, \varphi_v, \lambda) / \mathrm{E}_d(\lambda), \quad (1)$$

where $L_w(\theta_v, \varphi_v, \lambda)$ is the water leaving radiance, $E_d(\lambda)$ is the downwelling irradiance, θ_v, φ_v are the viewing (VA) and azimuth angles respectively and λ is the wavelength. Viewing angles are measured from nadir and the azimuth angle is equal to 0° when the Sun and the sensor are in opposition.

Optics EXPRESS

For above surface ocean observations, assuming that Sun glint is avoided and there are no whitecaps, $L_w(\theta_v,\varphi_v,\lambda)$ is determined from

$$L_t(\theta_v,\varphi_v,\lambda) = L_w(\theta_v,\varphi_v,\lambda) + \rho(\theta_v,\varphi_v,\lambda,W,AOT,\ldots)L_s(\pi-\theta_v,\varphi_v,\lambda), \qquad (2)$$

where $L_t(\theta_v,\varphi_v,\lambda)$ is the total upwelling radiance leaving the ocean surface, with a typical relative solar azimuth angle of $\phi_v = 90°$ or $\phi_v = 135°$ [18]. For a flat ocean surface, the ρ coefficient is the Fresnel coefficient defined by the viewing angle [37] and the indices of refraction of the air and water. In the presence of ocean waves it is a function of many parameters, including wind speed, illumination-viewing conditions, aerosol optical thickness (AOT), polarization, dispersion of seawater, and Sun glint [29–31,38,39] and is thus wavelength dependent. Generally ρ is the integral of reflections from individual wave facets, so it additionally depends on the FOV and the integration time of the sensor. For satellite observations at the top of atmosphere (TOA), surface effects are included in both the Rayleigh component (calculated independently of aerosol parameters) and in the radiances for aerosol models [16,40,41].

In this work, the RayXP vector radiative transfer code (VRT) [25] was used in RT closure with the measurements from the imager. This code was successfully benchmarked against other VRT codes [25,42], polarimetric measurements of the atmosphere-ocean system [43–45] and surface effects for wind roughened surface [31]. The code allows the stratification of the atmosphere and ocean in horizontally homogeneous (plane parallel) layers, which are characterized by molecular absorption (τ_{ABS}) and scattering (τ_{MOL}) optical depths, depolarization ratio, and an aerosol or hydrosol (represented by a 4x4 single-scattering Mueller matrix, single scattering albedo, and optical depth, τ_{SOL}).

The Stokes vectors corresponding to the radiance arriving at the sensor from the water body (L_t) and the sky (L_s) were computed from the simulations of the atmosphere-ocean system assuming a set of the following plane-parallel homogeneous layers. The first three layers are dedicated to the atmosphere (described top to bottom) with the first one representing 64.74% of the total Rayleigh optical thickness (τ_R) and 100% of the ozone optical thickness (τ_{O_3}), a middle layer containing the remaining 35% of τ_R and the full aerosol optical thickness, and the last layer with 0.26% of τ_R between the sensor and the ocean surface. The aerosol single scattering albedo was assumed 0.99 for all simulations. Aerosols are usually absorbing in the coastal areas and that can be the reason for some discrepancies. Rayleigh optical thickness values were the same as the ones used for MODIS products (0.098 at 550 nm). The middle layer containing aerosols was defined as consisting of a mixture of 79.6% sea salt, 19.9% dust and 0.5% soot by volume with a relative humidity of 60% [29]. The total aerosol optical thickness τ_A and Angstrom coefficient γ used for simulations were from Microtops II (Solar Light, PA) measurements. The oceanic layer, including hydrosols, was composed simply of one homogenous, optically thick water layer at which IOPs were measured (i.e. 0.5m underneath the water surface). The hydrosol single scattering albedo was calculated from the particulate absorption and attenuation. A Rayleigh depolarization factor of 0.039 was applied to account for the molecular anisotropy of water molecules [46]. Isotropic Cox-Munk slope distributions [20] were assumed for all simulations based on average anemometer wind speed (W) measurements. The variance σ_{iso}^2 of the isotropic slope distribution related to the wind speed W at 12.5 m above the surface level is determined as [20]

$$\sigma_{iso}^2 = 0.003 + 0.00512W \pm 0.004. \qquad (3)$$

Optics EXPRESS

The VRT program does not simulate uncertainties of L_t, L_w and ρ. Including 1-sigma uncertainties into the nomenclature, we now have

$$L_s \pm \sigma_s,\ L_t \pm \sigma_t,\ L_w \pm \sigma_w,\ \rho \pm \sigma_\rho, \tag{4}$$

where the $(\theta_v, \varphi_v, \lambda)$ parameters have been omitted for clarity, and σ_t, σ_w, σ_s and σ_ρ are the standard deviations of the total, water leaving and sky radiances, and reflectance coefficient, respectively. The full uncertainty equation for the total radiance (assuming lack of glint and foam in Eq. (2)) is given as [47]

$$\sigma_t^2 = \begin{bmatrix} \frac{\partial L_t}{\partial L_w} & \frac{\partial L_t}{\partial L_s} & \frac{\partial L_t}{\partial \rho} \end{bmatrix} \begin{bmatrix} \sigma_w^2 & \sigma_{ws} & \sigma_{w\rho} \\ \sigma_{ws} & \sigma_s^2 & \sigma_{s\rho} \\ \sigma_{w\rho} & \sigma_{s\rho} & \sigma_\rho^2 \end{bmatrix} \begin{bmatrix} \frac{\partial L_t}{\partial L_w} \\ \frac{\partial L_t}{\partial L_s} \\ \frac{\partial L_t}{\partial \rho} \end{bmatrix}, \tag{5}$$

where all covariance terms are included. The partial derivatives may be computed simply, resulting in $\frac{\partial L_t}{\partial L_w} = 1$, $\frac{\partial L_t}{\partial L_s} = \rho$ and $\frac{\partial L_t}{\partial \rho} = L_s$. Substituting the computed derivatives into Eq. (5) and simplifying, yields

$$\sigma_t^2 = \sigma_{w0}^2 + \rho^2\sigma_s^2 + L_s^2\sigma_\rho^2 + 2\rho L_s\sigma_{s\rho} + 2\rho\sigma_{ws} + 2L_s\sigma_{w\rho}. \tag{6}$$

In the above equation, σ_w^2 has been replaced with σ_{w0}^2, for contrast with an alternate formulation below. This equation identifies components which contribute to the variance of the total signal emanating from the ocean surface, and includes σ_{w0}^2, which is due to the natural variability of the upwelling radiance under the surface and its propagation through the wind-roughened water-air interface.

If we use Eq. (2) in the form of $L_w = L_t - \rho L_s$, the variance of the water leaving signal would then be

$$\sigma_w^2 = \sigma_t^2 + \rho^2\sigma_s^2 + L_s^2\sigma_\rho^2 + 2\rho L_s\sigma_{s\rho} - 2\rho\sigma_{ts} - 2L_s\sigma_{t\rho}. \tag{7a}$$

In this equation σ_w^2 characterizes the variance of L_w in the process of L_w retrieval from above surface measurements, depends on all components in Eq. (7a) and as such can be very different from σ_{w0}^2. Additional relationships regarding σ_{w0}^2 and σ_w^2 from Eqs. (6) and (7a) will be further given in Section 5.1.

Let us assume that σ_ρ in Eq. (7a) is small and ρ almost constant for a given measurement at a specific viewing angle. This is the typical practice for estimation of L_w *in situ*. In actuality, this is only a valid assumption under conditions of very low wind speed, homogenous sky, viewing angles near nadir, and solar angles near the horizon where the contribution of Sun glitter is small. Then

$$\sigma_w^2 \approx \sigma_t^2 + \rho^2\sigma_s^2 - 2\rho\sigma_{ts}, \tag{7b}$$

and through the subtraction of Eq. (7b) from (7a) and considering a weak correlation between ρ and L_s, we can estimate the effect of the assumption as

$$L_s^2\sigma_\rho^2 \approx 2L_s\sigma_{t\rho} \text{ or } \sigma_\rho \approx 2r_{t\rho}\sigma_t / L_s, \tag{7c}$$

Optics EXPRESS

where $r_{t\rho}$ is the correlation coefficient for L_t and ρ. Thus a preliminary relationship between σ_t and σ_ρ in Eq. (7c) can be established.

Using data from the imager we can quantify components σ_w, σ_t, σ_s, σ_{ts} as well as corresponding correlation coefficients in Eq. (7) to estimate realistic uncertainties in measurements of these parameters and contributions to the total signals. Due to the assumptions made, sometimes the value of $r_{t\rho}$ exceeds 1. In these cases, $r_{t\rho}$ was clamped to a value of 1.

As noted above, assumption of the constant coefficient ρ corresponds to typical cases of derivation of the water leaving radiance L_w using Eq. (2), as is done for above water measurements and in the satellite atmospheric correction models.

Since σ_ρ cannot be determined from Eq. (7), additional relationships based on Eq. (3) [20] were utilized to find a dependence of σ_ρ on the wind speed and viewing geometry. starting with the isotropic mean-square wave slope as a function of wind speed, σ_{iso}^2, the Gaussian probability density function describing the slope distribution, $f(x\,|\,\sigma_{iso}^2)$, is given by

$$f(x\,|\,\sigma_{iso}^2) = \left(2\pi\sigma_{iso}^2\right)^{-1/2} \exp\left(\frac{-x^2}{2\sigma_{iso}^2}\right), \tag{8}$$

where x is the slope. For calculation of the Fresnel coefficients, the slopes are converted to viewing angles (θ_n, the angle between zenith and the instantaneous "facet" normal direction) by $\theta_n = \tan^{-1}(x)$, and the incidence angle upon the facet (θ_{facet}) which would produce a reflection observable at a viewing angle of θ_v is determined by $\theta_{facet} = \theta_v + \theta_n$.

This simplified view ignores wave shadowing and multiple scattering by wave surfaces. These effects become significant at large VAs, where due to the simplification the possibility exists that $\theta_{facet} > 90°$, which is of course unphysical. For this calculation, the sky radiance is assumed to be isotropic, since skylight influence upon ρ is accounted for separately through the σ_s and $\sigma_{s\rho}$ terms. In this work we limit the VA to $\theta_v \le 60°$, which are anyhow the angles of interest for ocean color and largely mitigate the problem, but still may produce some small amounts of shadowing at the fringes of the slope distribution. Such angles are omitted from the calculation (since we are not accounting for multiple scattering by wave surfaces), but when this occurs $f(x)$ is renormalized in order to maintain the requirement that $\int_{-\infty}^{\infty} f(x)dx \equiv 1$.

Given the probability distribution, and the corresponding unpolarized Fresnel coefficients $\rho_F(\theta_{facet})$, we may then estimate the variance of the reflectance coefficient σ_ρ^2 for a given angle and wind speed by

$$\sigma_\rho^2(\theta_v, \sigma_{iso}^2) = \int_{-\infty}^{\infty} f(x)\rho_F^2 dx - \left(\int_{-\infty}^{\infty} f(x)\rho_F dx\right)^2. \tag{9}$$

Figure 4 illustrates the variation of σ_ρ as a function of VA, and the coefficient of variation σ_ρ / ρ for wind speeds of 2, 5, and 8 m/s.

Optics EXPRESS

The standard deviation of the sea surface reflectance, σ_ρ is shown in Fig. 4(a). The value is small at θ_v = 20° and lower, but rises to about 0.01 for the typical case of 40° and 5m/s winds, which is a variability of about 35%, Fig. 4(b). If we consider that the CV represents the 1-sigma variation, the 3-sigma variation is over 100%, which clearly shows that σ_ρ is the significant factor in the overall uncertainty budget, and becomes more so as the wind speed and viewing angle increases.

It should be noted that the distribution of ρ is not Gaussian [29], but the uncertainty propagation framework [47] described by Eq. (5) intrinsically assumes that all errors and uncertainties are Gaussian in nature. Without explicitly running Monte Carlo simulations to determine the exact distribution of all variables involved, all estimates of uncertainties given in this work are assumed to be Gaussian.

With all other terms now known, the spectra of covariances $\sigma_{t\rho}$ and corresponding correlation coefficients were determined from Eq. (7c).

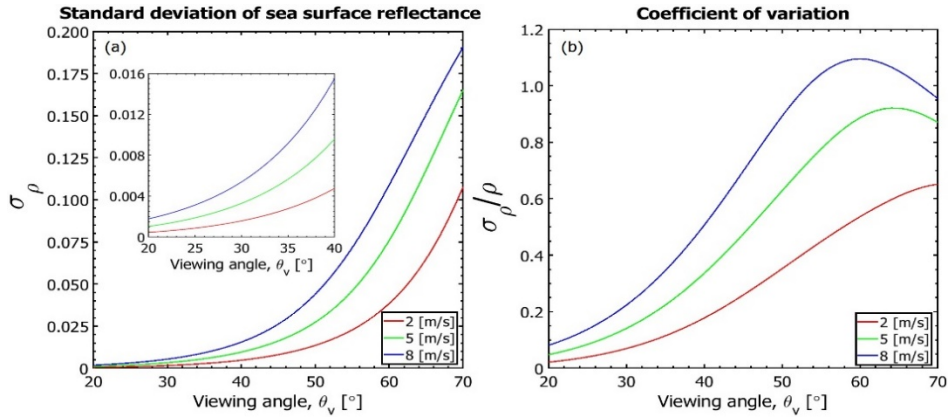

Fig. 4. Standard deviation σ_ρ and a coefficient of variation σ_ρ/ρ as a function of viewing angle for 2, 5, and 8 m/s wind speeds.

4. Field measurements

Above water observations were carried out from three coastal platforms: a) a 150-m long platform (Steeplechase pier, 40.5702° N, 73.9834° W) located in Brooklyn, NY; b) an offshore platform (Long Island Sound Coastal Observatory, LISCO, 40.9545° N, 73.3418° W) located 2 miles offshore from Northport, NY, and c) a 500-m long pier (US Army Corps of Engineers Field Research Facility (FRF), 36.1833° N, 75.7464° W) located in Duck, NC. Platform heights above mean sea level were 7m, 4m and 8m and bottom depth were 5 m, 15 m and 6 m, respectively. Total 14 measurements are considered in the processing with wind speed in the range of 3.0-5.7 m/s, Sun zenith angle SZA = 43-69°, AOT(440) = 0.198-0.452.

The imager was installed on a tripod as shown in Fig. 1(b), with its optical axis oriented at 40° from nadir for the observations of the water surface ($\theta_v = 40°$) and at 40° from zenith for sky observations ($\theta_v = 140°$). The relative solar azimuth angle was fixed at 90° or 270°, depending on measurement conditions. The imager's 40° FOV covered the range of viewing angles from 20° to 60° with respect to nadir (water-viewing) and zenith (sky-viewing). In the each measurement cycle, water and sky observations were complemented by measurements of the downwelling irradiance using a Spectralon white plate, and measurements of the dark noise. At the same time spectral data from the water, sky and the plate were acquired by a GER-1500 spectroradiometer, AOT was measured by a Microtops Sun-photometer at wavelengths 380, 500, 675, 870 and 1020 nm. Inherent Optical Properties (IOPs) of water

Optics EXPRESS

were measured *in situ* using an ac-s instrument (WET Labs, OR), except for the Brooklyn Pier, where water samples were measured in the CCNY laboratory using the same instrument. To obtain the appropriate measured IOPs from the ac-s system, correction of pure water, temperature, salinity, and scattering dependencies [48,49] were performed in the processing. Absorption of CDOM spectra was not measured directly for experiments at the FRF but was retrieved based on spectra measured by the GER-1500 instrument using a general coastal waters relationship which considers the phytoplankton and mineral absorption [50]. The GER-1500 spectra were corrected for the sky reflectance [18] with the reflectance coefficient $\rho = 0.028$ for W = 5 m/s and $\rho = 0.024$ for low wind conditions. Examples of the IOPs and remote sensing reflectance spectra measured at all three sites are shown in Fig. 5. Wind speed was measured by a handheld anemometer at NY sites and by permanently installed anemometers at the FRF in Duck.

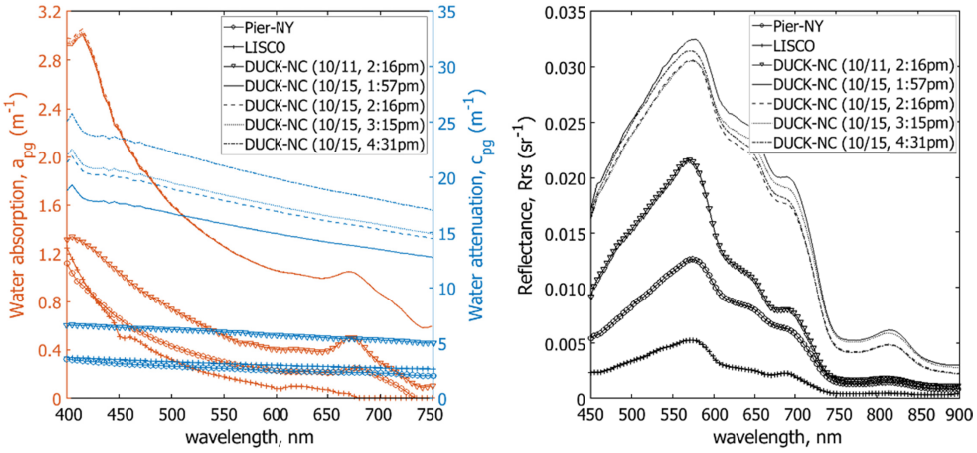

Fig. 5. Water IOPs and remote sensing reflectance spectra from the studied sites: (a) particulate + CDOM absorption 'a_{pg}' and attenuation 'c_{pg}', (b) remote sensing reflectance from GER. Data are shown for the Brooklyn Pier, 5/03/17, LISCO platform, 08/24/17, FRF Pier on 10/11/17 and 10/15/17.

The chlorophyll-a concentration [Chl-a] was estimated to be 3.0 mg/m^3 at the LISCO site and 14.0 mg/m^3 at the Duck site. Water IOPs and R_{rs} were highly variable and changed about five times depending on the water composition.

5. Results of measurements and comparison with VRT simulations

5.1 Radiance spatial distribution, estimation of uncertainties

The main advantage of the imager is the availability of the radiance spatial distribution over the FOV for each wavelength. The example of such data for three wavelengths for L_t, L_s and derived by Eq. (2) L_w is shown in Fig. 6 for the experiments from the FRF platform demonstrating radiance variability and opening the possibility for the statistical analysis of the radiance fluctuations both spectrally and spatially. Azimuth viewing angles φ_v are given for $\theta_v = 40°$ with values slightly different for other viewing angles. Corresponding panchromatic water and sky images are shown at the bottom of Fig. 6. It should be noticed that sky radiance has strong azimuth dependence. Coordinates θ_v and φ_v are shown for the center of the image; small differences in the scales at the different parts of the image were not taken into account. In all derivations of L_w here and below from measured L_t and L_s spectra was calculated based on Eq. (2) with the ρ coefficient from [18], except Fig. 7 where L_w was

Optics EXPRESS

determined from VRT by subtracting above surface radiances computed for fully absorbing ocean.

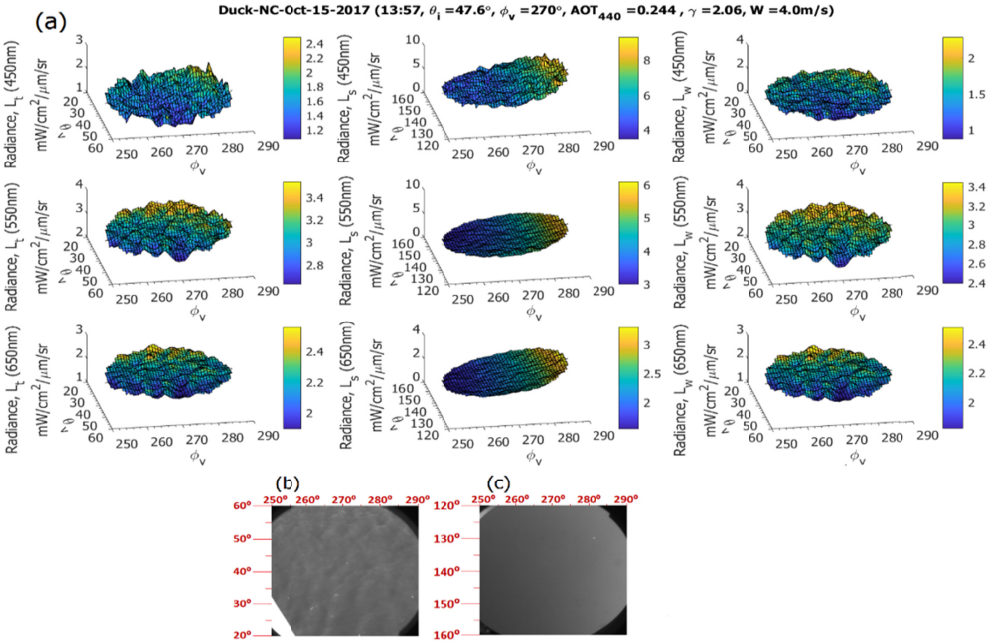

Fig. 6. (a) Pixel-to-pixel variability of L_t, L_s (left to right) for three different wavelengths: 450, 550 and 650 nm (top to bottom) and L_w calculated using Eq. (2), (b) corresponding panchromatic images of water surface and (c) sky.

Measured spectra for the whole range of viewing angles 20-60° were compared with VRT simulations. In such matchups mean spectra in the regions of interests (ROIs) corresponding to different VA as shown in Fig. 7, and their simulated counterparts were compared. Each ROI had 4° in zenith direction and 40° in azimuth direction.

All atmospheric ($\tau_R, \tau_A, \tau_{O_3}$, etc.) and water parameters (IOPs and hydrosol Mueller matrices) were used as input parameters for RayXP and data cubes were produced, which match the spectral and spatial resolution of the imager (50x50x113). For this study we limited the wavelength range to 450-900 nm. Results of the comparison for the FRF measurements at W = 5.6 m/s are shown in Fig. 7 demonstrating a good match for all viewing angles. Some mismatch after 750nm is probably due to the large bandwidths in the imager in this part of the spectra (Fig. 2), while simulations were carried out for the central wavelengths. Comparison were similar also for the other wind speeds thus showing that the average radiances can be well simulated by VRT, which properly takes into account effects of wind-roughened surface. For most stations, the spectra from the imager at $\theta_v = 40°$ matched well the spectra measured by GER instrument with some discrepancies due to the bandwidth differences shown in Fig. 2. Figure 7 mostly demonstrates consistency of matchups between VRT and imager radiances simultaneously for all viewing angles from the same IOP and sky data inputs. Slight differences can be due to uncertainty in input parameters like aerosol and hydrosol scattering matrices, which led to slightly elevated backscattering in simulations.

The advantage of the imager is that in addition to the mean values, variability of the radiances can be also estimated. Spectra of mean radiance values (shown here as L_t and L_s), standard deviations σ_t and σ_s for the water and sky data and corresponding ratios σ_t / L_t and σ_s / L_s for each viewing angle and averaged over FOV, for the case with wind speed W =

Optics EXPRESS

5.6 m/s are shown in Fig. 8. All values were calculated based on the ROIs' configuration shown in Fig. 7. Because of the strong gradient of L_s in the azimuth direction σ_s was determined from 5x5 pixel boxes, which was then averaged over ROI.

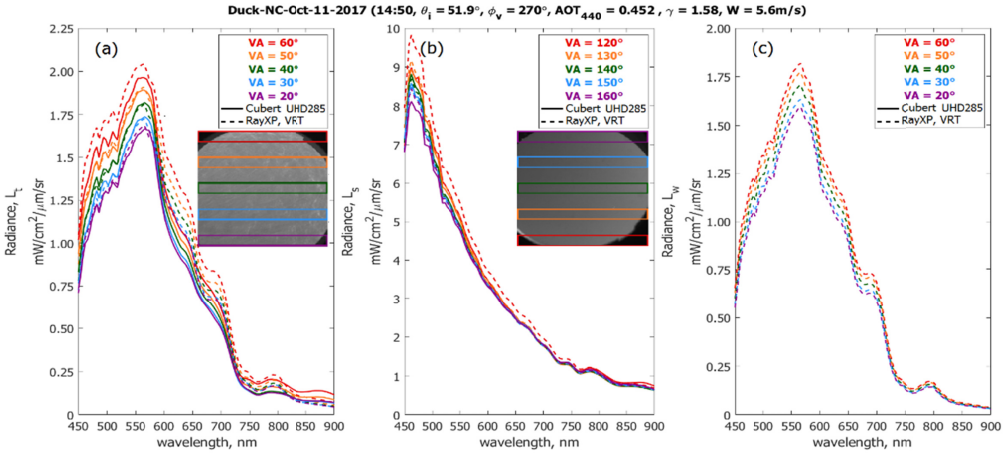

Fig. 7. Comparison of measurements and simulations for mean: (a) L_t , (b) L_s and (c) derived L_w at the FRF, 10/11/17. The insets denote the ROIs used throughout the rest of this work.

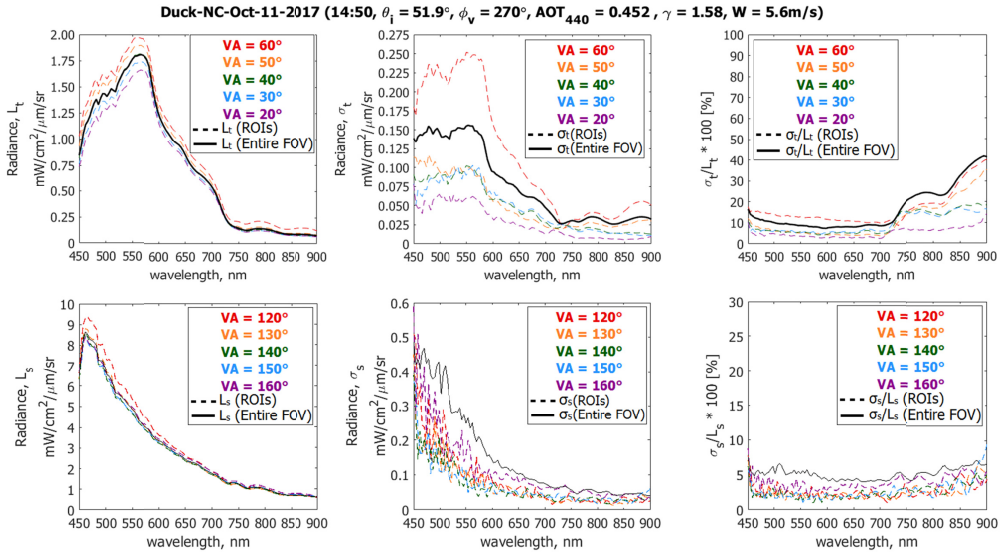

Fig. 8. Mean radiances L_t and L_s , standard deviations σ_t and σ_s for the water and sky data and corresponding ratios σ_t/L_t and σ_s/L_s for FRF station with wind speed W = 5.6 m/s.

Obviously all radiance values depend on the downwelling irradiance but in Fig. 8 absolute values are presented.

From Fig. 8 and similar data from other stations, σ_t/L_t is typically 5-15% depending on the viewing angle and noticeably increasing to 20-30% in the NIR with typically lowest values at 40° or smaller VA. σ_s/L_s is about 2-5% with a slight increase in the NIR. The contribution of different components in Eq. (7) were evaluated and as an example, measured and calculated spectra are presented for the same station in Fig. 9. In most cases σ_w is equal

Optics EXPRESS

or close to σ_t. The $\rho^2\sigma_s^2$ term was very small and is not shown in Fig. 9. $L_s^2\sigma_\rho^2 = 2L_s\sigma_{t\rho}$ is comparable with other terms for VA = 20-40° and becomes much higher at VA = 50-60° where assumption of small σ_ρ becomes inaccurate. But both parts of the equation probably remain similar, which makes $\sigma_w \approx \sigma_t$.

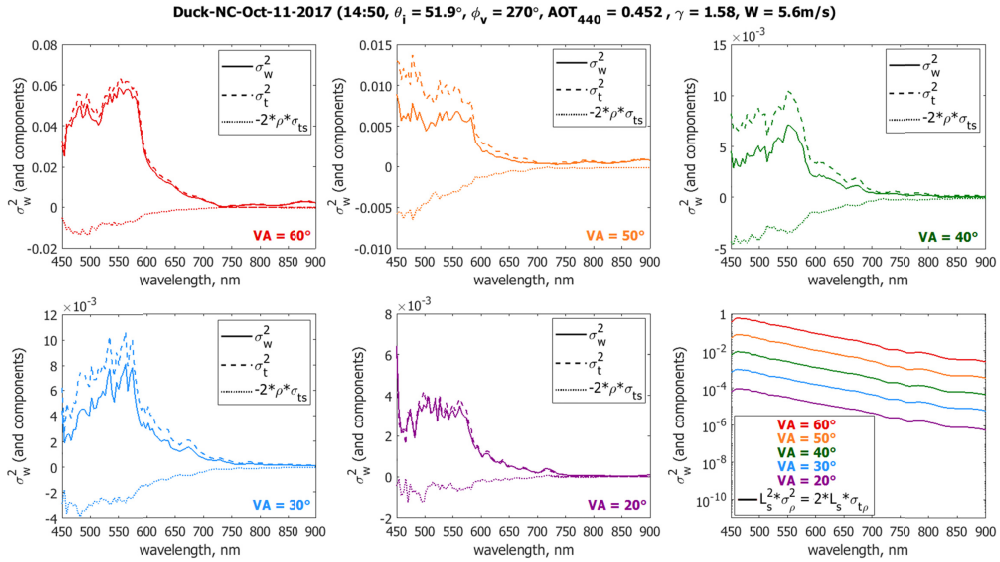

Fig. 9. Spectra of the main components from Eq. (7) for FRF station at different viewing angles in $(mW/cm^2/\mu m/sr)^2$. Bottom right figure is the $L_s^2\sigma_\rho^2 = 2L_s\sigma_{t\rho}$ term. The value of σ_w is determined in the assumption of constant ρ for all pixels in the same VA.

Table 1. Correlation coefficients $r_{t\rho}$ and r_{ts} for three stations

	$r_{t\rho}$			r_{ts}		
	LISCO (08/24/2017, 11:25, θi = 36.1°, w = 2.8 m/s)					
VA	470 nm	550 nm	650 nm	470 nm	550 nm	650 nm
40°	1.0	0.741	1.0	0.110	–0.364	–0.228
30°	0.368	0.287	0.285	–0.200	–0.350	–0.577
20°	0.141	0.087	0.090	0.283	0.563	0.491
	DUCK (10/15/2017, 14:16, θi = 49.3°, w = 4.2 m/s)					
VA	470 nm	550 nm	650 nm	470 nm	550 nm	650 nm
40°	0.154	0.081	0.071	0.642	0.715	0.612
30°	0.058	0.026	0.022	0.611	0.802	0.832
20°	0.014	0.008	0.007	0.454	0.501	0.561
	DUCK (10/11/2017, 14:50, θi = 51.9°, w = 5.6 m/s)					
VA	470 nm	550 nm	650 nm	470 nm	550 nm	650 nm
40°	0.530	0.255	0.315	0.812	0.920	0.851
30°	0.216	0.099	0.104	0.651	0.733	0.777
20°	0.083	0.047	0.061	0.370	0.306	0.343

The correlation coefficients $r_{t\rho}$ and r_{ts} for three stations are given in Table 1 for VA = 20-40° showing large variability as a function of viewing angle, wavelength and wind speed. Some inaccuracies in calculations of $r_{t\rho}$ could arise from the assumption of small σ_ρ in Eq. (7), which also resulted in $|r| > 1$ in two cases shown as $|r| = 1.0$ in the table.

Analysis of data for all available stations resulted in the coefficient of variation (CV) σ_w/L_w as a function of wind speed as shown in Fig. 10. The ratio is in the range of 3-8% for

Optics EXPRESS

most of viewing angles with increase to 6-20% in the NIR and higher for VA = 60° and small increase towards short wavelengths.

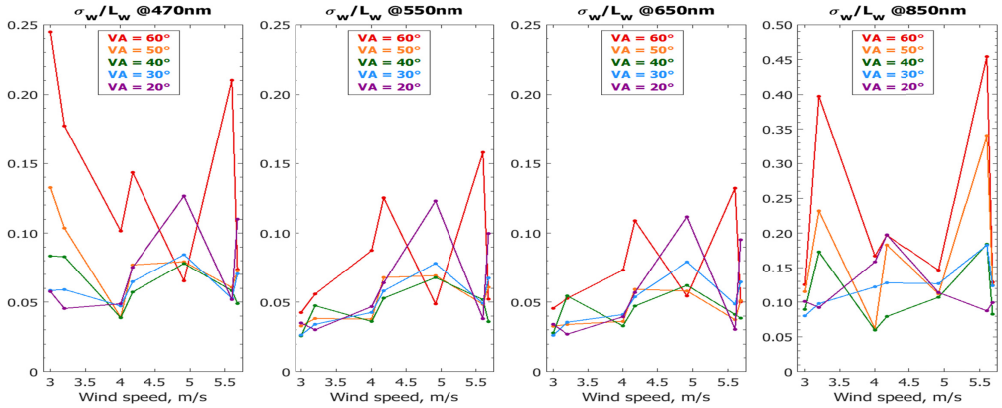

Fig. 10. The coefficient of variation for water-leaving radiance (σ_w/L_w) as a function of wind speed and viewing angle: 470nm, 550nm, 650nm and 850nm (left to right). σ_w is determined in the assumption of constant ρ for all pixels in the same VA.

As discussed above, $\rho^2\sigma_s^2$ term is typically very small in comparison with other components in Eq. (7) and similar ones in Eq. (6), also in Eq. (6) σ_w and σ_s are uncorrelated, which makes $2\rho\sigma_{ws} \approx 0$, a weak correlation can be expected between reflectance coefficient and sky radiance, so $2\rho L_s\sigma_{s\rho}$ term can be also omitted. Then Eq. (6) can be rewritten as

$$\sigma_t^2 = \sigma_{w0}^2 + L_s^2\sigma_\rho^2 + 2L_s\sigma_{w\rho}. \tag{10}$$

The main effect of sky glint comes from $L_s^2\sigma_\rho^2$ term but preliminary data analysis (omitted here for brevity) showed that covariance term also plays significant role depending on the viewing angle, which results in the partial mitigation of the sky glint; additional studies are required for a proper characterization of the σ_{w0}^2 and $\sigma_{w\rho}$ covariance.

Although the imager is unable to acquire data below 450 nm, we can estimate propagation of σ_w/L_w to the blue part of the spectrum. As shown in Fig. 9, $\sigma_w \approx \sigma_t$ and according to Eq. (10) at least partially proportional to $\sigma_\rho L_s$. Then we can write

$$\frac{\sigma_w}{L_w} \approx \frac{L_s}{L_w} = \frac{L_s}{E_d}\left(\frac{L_w}{E_d}\right)^{-1} = \frac{L_s}{E_d R_{rs}}. \tag{11}$$

In the open ocean, since the spectral shapes of the sky L_s/E_d and remote sensing reflectance R_{rs} are similar, the uncertainty for wavelengths near 400 nm will be only slightly higher than that of 450 nm. In the coastal waters, R_{rs} decreases rapidly till 400 nm. These effects are explained in Fig. 11 (for typical open ocean and coastal water spectra not acquired in this study) where L_s/L_w remains almost the same for the open ocean and increases towards the blue in the coastal waters. The result is a higher uncertainty σ_w/L_w in the blue wavelengths in the coastal waters. It is expected that the actual increase of σ_w/L_w can be smaller than shown in Fig. 11 because of contributions of other terms in Eq. (10) beyond $L_s^2\sigma_\rho^2$. These results are consistent with the spectra of R_{rs} variations measured in Chesapeake

Optics EXPRESS

Bay and Florida waters [53], Fig. 12. The σ_w/L_w ratio also increases towards the NIR part of the spectrum and even normalized sky radiance is small, this ratio can be partially responsible for the increase of uncertainties in the NIR as shown in Fig. 10.

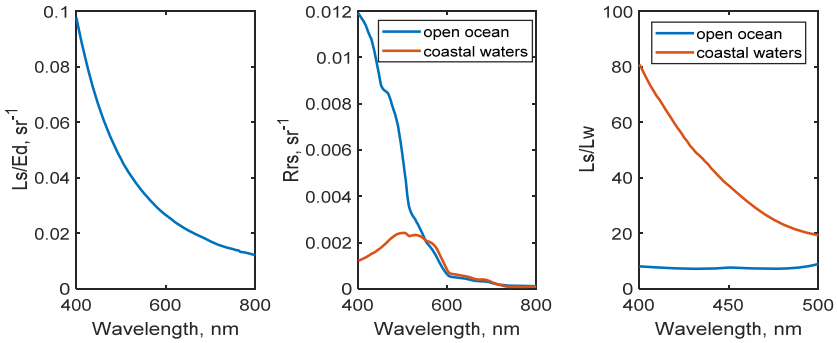

Fig. 11. (a) Normalized sky radiance spectrum,(b) R_{rs} and (c) their ratio for the open ocean and coastal waters.

5.2 Field of view considerations in above water measurements

Instruments which are used for L_t and L_s measurements above water have different FOV, ranging from about 1° (SeaPRISM) to greater than 20° (fiber optic sensors), so it is important to determine the dependence of L_t and L_s on the FOV and how it affects the mean radiances and their fluctuations in variable surface and sky conditions. L_t and L_s were measured at 40° and 140° viewing angles respectively, with a full-angle FOV (θ_{FOV}) up to 35° were calculated using the following expression:

$$L_{t,s}(\lambda,\Omega_{FOV}) = \frac{1}{\Omega_{FOV}} \iint_{\Omega_{FOV}} L_i(\lambda) d\Omega'_{FOV}, \tag{12}$$

where $L_{t,s}$ is the radiance for water and sky (L_t and L_s, respectively), Ω_{FOV} is the solid angle corresponding to the conical FOV and L_i is the radiance for each individual pixel within the FOV. Example of the spectra for different FOVs is shown for W = 4.5 m/s in Fig. 12 with the corresponding images and analyzed areas. It can be clearly seen that in the wide range of $\theta_{FOV} = 0.8° - 31.2°$ for the moderate wind speed there is very small dependence of radiance on the FOV for both L_t and L_s for the whole spectra.

Optics EXPRESS

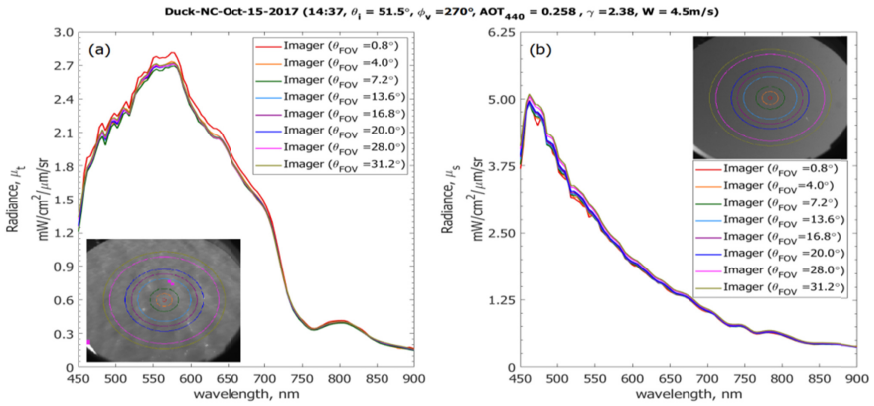

Fig. 12. (a) L_t and (b) L_s measured at 40° and 140° viewing angles as a function of FOV. The pink boxes in the image indicate saturated pixels which were excluded from the processing.

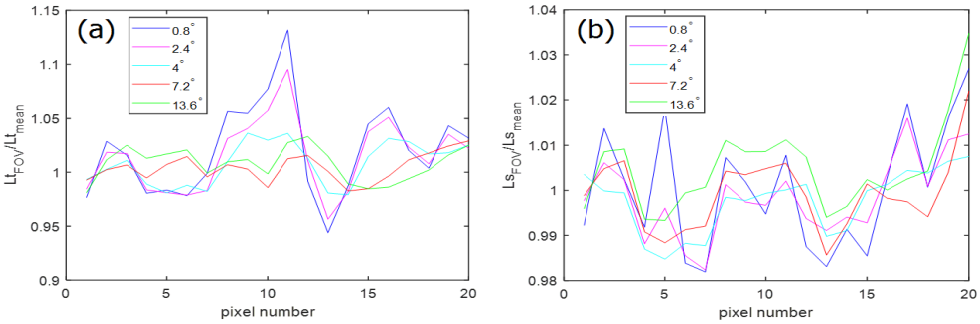

Fig. 13. Variability of L_{t_FOV}/L_{t_mean} and L_{s_FOV}/L_{s_mean} ratio for different θ_{FOV} , W = 4.5 m/s (Duck 14:37): (a) for water radiance, (b) for sky radiance.

To provide more information on the FOV radiance dependence, variability of radiance L_t at 530 nm was analyzed for measurements from the FRF platform at W = 4.5 m/s. Results are shown in Fig. 13(a) for 18 different pixels along the diagonal of the image, for which FOVs up to $\theta_{FOV} = 13.6°$ were tested. L_{t_FOV} radiance is normalized to the mean radiance L_{t_mean} determined from the 9 radiances (from the center pixel of study and ± 4 pixels closest to it along the horizontal line). It can be seen that starting with $\theta_{FOV} = 4°$ there is no noticeable dependence on the FOV where L_{t_FOV}/L_{t_mean} deviations are inside $\pm 3\%$, while smaller FOV provide less stable results. Analysis of sky measurements, Fig. 13(b), resulted in the same preferred FOV range where L_{s_FOV}/L_{s_mean} deviations are inside $\pm 2\%$. Statistics are presented only for one water and one sky image, but results were similar for many stations with different conditions with most stable results for $\theta_{FOV} = 4-7°$. The highest deviations are at $\theta_{FOV} = 0.8-2.4°$, which are most likely underestimated due to stray light from adjacent pixels causing increased pixel-to-pixel covariance and therefore reducing the deviations.

6. Implications for field measurements, AERONET-OC and satellite observations

In above water measurements from ships at 40° and 140° viewing angles, as it was shown previously [31], the mean value of the reflectance coefficient ρ depends on the wind speed, wavelength, AOT and polarization effects. This impact can be minimized if AOT is measured

Optics EXPRESS

and spectral ρ calculated accordingly. The coefficient of variation for water-leaving radiance (σ_w/L_w) is expected to be about 3-8% with increase to 6-20% in the NIR at $\theta_v = 40°$ and W < 6 m/s. According to Eq. (11) and Fig. 11 it is expected that σ_w/L_w remains approximately the same in the open ocean with increasing R_{rs} towards the blue end of the spectrum and increases in the coastal waters with decrease of R_{rs} causing larger measurement uncertainties. This trend was verified in the preliminary manner by us with the imager sensitive in the blue wavelength range and by AERONET-OC data and should be further validated. Partially the errors can be made smaller by increasing the number of measurements; however, this can often be associated with additional effects of the ship movements and instantaneous changes in sky and water conditions.

AERONET-OC measurements are carried out by SeaPRISM instruments at 40° and 140° viewing angles for the water and sky radiance respectively with an integration time of about 80 ms and a FOV of 1.2° [33]. An azimuth angle of ± 90° is always maintained to minimize Sun glint. Additional data filtering by eliminating cases with standard deviations σ_t greater than certain threshold is applied to reduce further Sun glint effects [51]. Instruments are positioned on the stable platforms in the ocean, which are not sensitive to the wave perturbations, so the increased number of measurements is expected to bring L_t closer to the mean value L_{t_mean}. L_w is then determined based on Eq. (2) with the ρ coefficient from [18], which was calculated without taking into account impacts of polarization and AOT. Estimations of σ_w/L_w from Fig. 10 and σ_t/L_t from Fig. 8 at $\theta_v = 40°$ are generally consistent with the AERONET-OC results based on data from several platforms [52]. While for $\theta_v = 40°$ $\sigma_\rho/\rho \approx 0.35$ (see Fig. 4) (if $\rho = 0.028$ is assumed), which is substantially higher than other estimations of σ_ρ/ρ calculated based on different reasons of ρ variability [52], these effects are probably mitigated by the covariance terms in Eq. (7).

In the current processing, L_t is taken to be the average of the lowest 2 out of 11 measurements, denoted as L_{t_REL}, which typically has a value between L_{t_mean} and $L_t^{'} = L_t - \sigma_t$. Data from the imager show that $L_t^{'}$ can be smaller than L_{t_mean} for $\theta_v = 40°$ depending on the wind speed and SZA. Further dedicated studies are probably necessary to determine possible improvements of L_w retrieval. This includes application of a proper ρ coefficient, which is preferably determined by VRT with aerosol parameters measured by the same AERONET-OC station. It is expected that in the new version of AERONET-OC processing ρ will be calculated taking into account aerosol and polarization effects [Zibordi, private communications].

It can be expected that standard deviations similar to $\sigma_t(\lambda)$ spectra determined in this work can characterize the uncertainties of the radiance at the TOA $L_{TOA}(\lambda)$, which are due to the effects of the ocean surface. In accordance with Eq. (11) and Fig. 11, σ_w/L_w is larger in the blue bands in the coastal waters than in the open ocean, which will contribute to the uncertainties of L_w and R_{rs}, derived from satellite observations. The uncertainties can be even further amplified by the dependence of ρ on AOT discussed in [31] with AOT very variable in coastal waters and not determined accurately enough in the atmospheric correction process.

Snapshot hyperspectral imagers like the one presented in this paper, which preferably covers the whole wavelength range of OC interest in at least 380-900 nm should be a suitable choice for the validation of the discussed effects in various water an atmospheric conditions.

Optics EXPRESS

7. Conclusions

A novel hyperspectral imager is introduced for OC applications in coastal waters and its advantages over non-imaging spectroradiometers and push broom imagers are discussed. The instrument provides hyperspectral radiance distribution with a wide FOV and short exposure time, which is valuable for the direct characterization of the wind-roughened surface in various illumination conditions and wind speeds. Spectra of standard deviations for the radiance from the water and the sky at the viewing angles 20-60° are accurately determined and their ratios to the corresponding mean radiances are evaluated, showing that the coefficients of variation $\sigma_t(\lambda)/L_t(\lambda)$ for water and $\sigma_s(\lambda)/L_s(\lambda)$ for the sky measurements can be in the range of 3-20% depending on the viewing angle, wind speed and wavelength.

The minimal values of $\sigma_t(\lambda)/L_t(\lambda)$ are typically around viewing angle of 40°or smaller VA. The coefficients of variation $\sigma_w(\lambda)/L_w(\lambda)$ is in the range of 3-8% for most cases and can reach 10-25% for VA = 60° at 470 nm. It is expected that $\sigma_w(\lambda)/L_w(\lambda)$ is higher in the blue bands in coastal waters, which at least partially explains typically inaccurate satellite retrieval of L_w in blue bands in such areas, where values of L_w are few times smaller than in the open ocean. Significant part of uncertainties comes from the variability of ρ coefficient from the windy surface (or its equivalent value from VRT calculations for TOA). It was found that σ_ρ/ρ can be about 35% at 40° and W = 5 m/s and about 100% at higher wind speed and VA = 60°. The uncertainties can be amplified by the dependence of ρ on AOT [31]. Thus accurate determination of the ρ coefficient, which takes into account polarization effects and impact of AOT is critical to the calculation of the water leaving radiance $L_w(\lambda)$, however, most of uncertainties come from the changes of wave slopes in windy conditions and can be unavoidable.

Further measurements with the imager in open ocean water conditions with different ocean states are suggested to analyze differences in surface effects between the near shore and open ocean areas, which can be directly relevant to satellite data processing in terms of atmospheric correction and retrieval algorithms.

Funding

National Aeronautics and Space Administration (NASA), Ocean Biology and Biochemistry program (NNX16AR46G); National Oceanic and Atmospheric Administration (NOAA), Joint Polar Satellite System Calibration/validation program and ESSRST Center (NA16SEC4810008); Office of Naval Research (ONR) (N00014-16-1-2555).

Acknowledgments

This research was performed while Robert Foster held an NRC Research Associateship award at the U.S. Naval Research Laboratory in Washington, DC. The authors are grateful for two anonymous reviewers whose suggestions significantly improved the quality of the paper. We thank Eder Herrera for processing auxiliary data.

References

1. C. Giardino, V. E. Brando, P. Gege, N. Pinnel, E. Hochberg, E. Knaeps, I. Reusen, R. Doerffer, M. Bresciani, F. Braga, S. Foerster, N. Champollion and A. Dekker, "Imaging spectrometry of inland and coastal waters: state of the art, achievements and perspectives" (Serv. Geophys., 2018). https://doi.org/10.1007/s10712-018-9476-0
2. C. D. Mobley, L. K. Sundman, C. O. Davis, J. H. Bowles, T. V. Downes, R. A. Leathers, M. J. Montes, W. P. Bissett, D. D. R. Kohler, R. P. Reid, E. M. Louchard, and A. Gleason, "Interpretation of hyperspectral remote-sensing imagery by spectrum matching and look-up tables," Appl. Opt. **44**(17), 3576–3592 (2005).
3. C. Davis, J. Bowles, R. Leathers, D. Korwan, T. V. Downes, W. Snyder, W. Rhea, W. Chen, J. Fisher, P. Bissett, and R. A. Reisse, "Ocean PHILLS hyperspectral imager: design, characterization, and calibration," Opt. Express **10**(4), 210–221 (2002).

Optics EXPRESS

4. E. J. Hochberg and M. J. Atkinson, "Spectral discrimination of coral reef benthic communities," Coral Reefs **19**(2), 164–171 (2000).
5. H. M. Dierssen, R. C. Zimmerman, R. A. Leathers, T. V. Downes, and C. O. Davis, "Ocean color remote sensing of seagrass and bathymetry in the Bahamas Banks by high resolution airborne imagery," Limnol. Oceanogr. **48**(1part2), 444–455 (2003).
6. J. C. Sandidge and R. J. Holyer, "Coastal bathymetry from hyperspectral observations of water radiance," Remote Sens. Environ. **65**(3), 341–352 (1998).
7. Z. P. Lee, K. L. Carder, R. F. Chen, and T. G. Peacock, "Properties of the water column and bottom derived from Airborne Visible Infrared Imaging Spectrometer (AVIRIS) data," J. Geophys. Res. **106**(C6), 11639–11651 (2001).
8. R. L. Lucke, M. Corson, N. R. McGlothlin, S. D. Butcher, D. L. Wood, D. R. Korwan, R. R. Li, W. A. Snyder, C. O. Davis, and D. T. Chen, "Hyperspectral Imager for the Coastal Ocean: instrument description and first images," Appl. Opt. **50**(11), 1501–1516 (2011).
9. P. Mouroulis, B. Van Gorp, R. Green, M. Eastwood, D. Wilson, B. Richardson, and H. Dierssen, "The Portable Remote Imaging Spectrometer (PRISM) Coastal Ocean Sensor," in Imaging and Applied Optics Technical Papers, OSA Technical Digest (online) (Optical Society of America, 2012), paper RM2E.5.
10. A. A. Gitelson, B.-C. Gao, R.-R. Li, S. Berdnikov, and V. Saprygin, "Estimation of chlorophyll-a concentration in productive turbid waters using a Hyperspectral Imager for the Coastal Ocean – the Azov Sea case study," Environ. Res. Lett. **6**(2), 024023 (2011).
11. PACE Science Definition Team, "Pre-Aerosol, Clouds, and ocean Ecosystem (PACE) mission science definition team report," http://decadal.gsfc.nasa.gov/.
12. A. Ibrahim, B. Franz, Z. Ahmad, R. Healy, K. Knobelspiesse, B.-C. Gao, C. Proctor, and P.-W. Zhai, "Atmospheric correction for hyperspectral ocean color retrieval with application to the Hyperspectral Imager for the Coastal Ocean (HICO)," Remote Sens. Environ. **204**, 60–75 (2018).
13. D. R. Mishra and I. Ogashawara, *Bio-Optical Modeling and Remote Sensing of Inland Waters* (Elsevier, 2017), pp. 69–100.
14. C. Carrizo, A. Golovin, A. El-Habashi, R. Foster, D. Gray, J. Bowles, and A. Gilerson, "Ocean surface characterization using snapshot hyperspectral polarimetric imager," Proc. SPIE **10631**, 1063107 (2018).
15. H. R. Gordon and M. Wang, "Surface-roughness considerations for atmospheric correction of ocean color sensors. I: The Rayleigh-scattering component," Appl. Opt. **31**(21), 4247–4260 (1992).
16. H. R. Gordon and M. Wang, "Retrieval of water-leaving radiance and aerosol optical thickness over the oceans with SeaWiFS: a preliminary algorithm," Appl. Opt. **33**(3), 443–452 (1994).
17. M. Wang, "The Rayleigh lookup tables for the SeaWiFS data processing: accounting for the effects of ocean surface roughness," Int. J. Remote Sens. **23**(13), 2693–2702 (2002).
18. C. D. Mobley, "Estimation of the remote-sensing reflectance from above-surface measurements," Appl. Opt. **38**(36), 7442–7455 (1999).
19. J. L. Mueller, A. Morel, R. Frouin, C. Davis, R. Arnone, K. Carder, Z .P. Lee, R. G. Steward, S. Hooker, C. D. Mobley, S. McLean, B. Holben, M. Miller, C. Pietras, K. D. Knobelspiesse, G. S. Fargion, J. Porter, and K. Voss, "*Ocean Optics Protocols for Satellite Ocean Color Sensor Validation, Revision 4, Volume III: Radiometric Measurements and Data Analysis Protocols*" (Goddard Space Flight Space Center, 2003).
20. C. Cox and W. Munk, "Measurement of the roughness of the sea surface from photographs of the sun's glitter," J. Opt. Soc. Am. **44**(11), 838–850 (1954).
21. C. D. Mobley, L. K. Sundman, HYDROLIGHT 4.2, Sequoia Scientific, Inc. (2001).
22. J. Chowdhary, B. Cairns, and L. D. Travis, "Contribution of water-leaving radiances to multiangle, multispectral polarimetric observations over the open ocean: bio-optical model results for case 1 waters," Appl. Opt. **45**(22), 5542–5567 (2006).
23. M. Chami, R. Santer, and E. Dilligeard, "Radiative transfer model for the computation of radiance and polarization in an ocean-atmosphere system: polarization properties of suspended matter for remote sensing," Appl. Opt. **40**(15), 2398–2416 (2001).
24. C. D. Mobley, "Polarized reflectance and transmittance properties of windblown sea surfaces," Appl. Opt. **54**(15), 4828–4849 (2015).
25. H. H. Tynes, G. W. Kattawar, E. P. Zege, I. L. Katsev, A. S. Prikhach, and L. I. Chaikovskaya, "Monte Carlo and multi-component approximation methods for vector radiative transfer by use of effective Mueller matrix calculations," Appl. Opt. **40**(3), 400–412 (2001).
26. P.-W. Zhai, Y. Hu, J. Chowdhary, C. R. Trepte, P. L. Lucker, and D. B. Josset, "A vector radiative transfer model for coupled atmosphere and ocean systems with a rough interface," J. Quant. Spectrosc. Radiat. Transf. **111**(7–8), 1025–1040 (2010).
27. B. Fougnie, R. Frouin, P. Lecomte, and P. Y. Deschamps, "Reduction of skylight reflection effects in the above-water measurement of diffuse marine reflectance," Appl. Opt. **38**(18), 3844–3856 (1999).
28. Z. Lee, Y.-H. Ahn, C. Mobley, and R. Arnone, "Removal of surface-reflected light for the measurement of remote-sensing reflectance from an above-surface platform," Opt. Express **18**(25), 26313–26324 (2010).
29. R. Foster and A. Gilerson, "Polarized transfer functions of the ocean surface for above-surface determination of the vector submarine light field," Appl. Opt. **55**(33), 9476–9494 (2016).
30. X. Zhang, S. He, A. Shabani, P. W. Zhai, and K. Du, "Spectral sea surface reflectance of skylight," Opt. Express **25**(4), A1–A13 (2017).

Optics EXPRESS

31. A. Gilerson, C. Carrizo, R. Foster, and T. Harmel, "Variability of the reflectance coefficient of skylight from the ocean surface and its implications to Ocean Color," Opt. Express **26**(8), 9615–9633 (2018).
32. A. Gilerson, E. Herrera, Y. Klein, R. Foster, B. Gross, R. Arnone, and S. Ahmed, "Characterization of aerosol parameters over ocean from the Ocean Color satellite sensors and AERONET-OC data," Proc. SPIE **10422**, 104220H (2017).
33. G. Zibordi, F. Mélin, J. F. Berthon, B. Holben, I. Slutsker, D. Giles, D. D'Alimonte, D. Vandemark, H. Feng, G. Schuster, B. E. Fabbri, S. Kaitala, and J. Seppälä, "AERONET-OC: a network for the validation of ocean color primary products," J. Atmos. Ocean. Technol. **26**(8), 1634–1651 (2009).
34. H. Aasen, A. Burkart, A. Bolten, and G. Bareth, "Generating 3D hyperspectral information with lightweight UAV snapshot cameras for vegetation monitoring: From camera calibration to quality assurance," J. Photog. Remote Sens. **108**, 245–259 (2015).
35. C. J. Zappa, M. L. Banner, H. Schultz, A. Corrada-Emmanuel, L. B. Wolff, and J. Yalcin, "Retrieval of short ocean wave slope using polarimetric imaging," Meas. Sci. Technol. **19**(5), 055503 (2008).
36. C. D. Mobley, *Ocean Optics Web Book*, http://www.oceanopticsbook.info/
37. E. Hecht, *Optics*, (Pearson Education, 2009).
38. X. Quan and E. S. Fry, "Empirical equation for the index of refraction of seawater," Appl. Opt. **34**(18), 3477–3480 (1995).
39. T. Harmel, A. Gilerson, A. Tonizzo, J. Chowdhary, A. Weidemann, R. Arnone, and S. Ahmed, "Polarization impacts on the water-leaving radiance retrieval from above-water radiometric measurements," Appl. Opt. **51**(35), 8324–8340 (2012).
40. C. D. Mobley, J. Werdell, B. Franz, Z. Ahmad and S. Bailey "*Atmospheric Correction for Satellite Ocean Color Radiometry*," (Goddard Space Flight Space Center, 2016).
41. Z. Ahmad, B. A. Franz, C. R. McClain, E. J. Kwiatkowska, J. Werdell, E. P. Shettle, and B. N. Holben, "New aerosol models for the retrieval of aerosol optical thickness and normalized water-leaving radiances from the SeaWiFS and MODIS sensors over coastal regions and open oceans," Appl. Opt. **49**(29), 5545–5560 (2010).
42. A. Kokhanovsky, V. P. Budak, C. Cornet, M. Duan, C. Emde, I. L. Katsev, D. A. Klyukov, S. V. Korkin, L. C-Labonnote, B. Mayer, Q. Min, T. Nakajima, Y. Ota, A. S. Prikhach, V. V. Rozanov, T. Yokota, and E. P. Zege, "Benchmark results in vector atmospheric radiative transfer," J. Quant. Spectrosc. Radiat. Transf. **111**(12–13), 1931–1946 (2010).
43. A. A. Gilerson, J. Stepinski, A. I. Ibrahim, Y. You, J. M. Sullivan, M. S. Twardowski, H. M. Dierssen, B. Russell, M. E. Cummings, P. Brady, S. A. Ahmed, and G. W. Kattawar, "Benthic effects on the polarization of light in shallow waters," Appl. Opt. **52**(36), 8685–8705 (2013).
44. P. C. Brady, A. A. Gilerson, G. W. Kattawar, J. M. Sullivan, M. S. Twardowski, H. M. Dierssen, M. Gao, K. Travis, R. I. Etheredge, A. Tonizzo, A. Ibrahim, C. Carrizo, Y. Gu, B. J. Russell, K. Mislinski, S. Zhao, and M. E. Cummings, "Open-ocean fish reveal an omnidirectional solution to camouflage in polarized environments," Science **350**(6263), 965–969 (2015).
45. M. Ottaviani, R. Foster, A. Gilerson, A. Ibrahim, C. Carrizo, A. El-Habashi, B. Cairns, J. Chowdhary, C. Hostetler, J. Hair, S. Burton, Y. Hu, M. Twardowski, N. Stockley, D. Gray, W. Slade, and I. Cetinic, "Airborne and shipborne polarimetric measurements over open ocean and coastal waters: intercomparisons and implications for spaceborne observations," Remote Sens. Environ. **206**, 375–390 (2018).
46. R. S. Farinato and R. L. Rowell, "New values of the light scattering depolarization and anisotropy of water," J. Chem. Phys. **65**(2), 593–595 (1976).
47. A. Bevan, *Statistical Data Analysis for the Physical Sciences*, (Cambridge University, 2013).
48. J. M. Sullivan, M. S. Twardowski, J. R. V. Zaneveld, C. M. Moore, A. H. Barnard, P. L. Donaghay, and B. Rhoades, "Hyperspectral temperature and salt dependencies of absorption by water and heavy water in the 400-750 nm spectral range," Appl. Opt. **45**(21), 5294–5309 (2006).
49. N. D. Stockley, R. Röttgers, D. McKee, I. Lefering, J. M. Sullivan, and M. S. Twardowski, "Assessing uncertainties in scattering correction algorithms for reflective tube absorption measurements made with a WET Labs ac-9," Opt. Express **25**(24), A1139–A1153 (2017).
50. D. R. Mishra, I. Ogashawara, and A. A. Gitelson, *Bio-Optical Modeling And Remote Sensing Of Inland Waters* (Elsevier, 2017), pp. 189–231.
51. G. Zibordi, "Comment on "Long Island Sound Coastal Observatory: assessment of above-water radiometric measurement uncertainties using collocated multi and hyperspectral systems"," Appl. Opt. **51**(17), 3888–3892 (2012).
52. M. Gergely and G. Zibordi, "Assessment of AERONET-OC Lwn uncertainties," Metrologia **51**(1), 40–47 (2014).
53. M. Zhang, C. Hu, J. Cannizzaro, D. English, B. B. Barnes, P. Carlson, and L. Yarbro, "Comparison of two atmospheric correction approaches applied to MODIS measurements over North American waters," Remote Sens. Environ. **216**, 442–455 (2018).